Journal of Magnetic Resonance 194 (2008) 245–253

Contents lists available at ScienceDirect

Journal of Magnetic Resonance

journal homepage: www.elsevier.com/locate/jmr

# Spatial and temporal mapping of water content across Nafion membranes under wetting and drying conditions

Ziheng Zhang [a], Andrew E. Marble [a,1], Bryce MacMillan [a], Keith Promislow [b], Jonathan Martin [c], Haijiang Wang [c], Bruce J. Balcom [a,*]

[a] MRI Centre, Department of Physics, University of New Brunswick, Post Office Box 4400 I.U.C., Fredericton, NB, Canada E3B 5A3
[b] Department of Mathematics, Michigan State University, East Lansing, MI 48824, USA
[c] Institute for Fuel Cell Innovation (IFCI), National Research Council Canada (NRC), 4250 Wesbrook Mall, Vancouver, BC, Canada V6T 1W5

ARTICLE INFO

*Article history:*
Received 7 January 2008
Revised 10 July 2008
Available online 17 July 2008

*Keywords:*
Water content
Water transport
Water management
MRI
Nafion
Fuel cell
Spin echo SPI

ABSTRACT

Water transport and water management are fundamental to polymer electrolyte membrane fuel cell operation. Accurate measurements of water content within and across the Nafion layer are required to elucidate water transport behavior and validate existing numerical models.

We report here a direct measurement of water content profiles across a Nafion layer under wetting and drying conditions, using a novel magnetic resonance imaging methodology developed for this purpose. This method, multi-echo double half k-space spin echo single point imaging, based on a pure phase encode spin echo, is designed for high resolution 1D depth imaging of thin film samples. The method generates high resolution (<8 μm) depth images with an SNR greater than 20, in an image acquisition time of less than 2 min. The high temporal resolution permits water content measurements in the transient states of wetting and drying, in addition to the steady state.



## 1. Introduction

Polymer electrolyte membrane (PEM) fuel cells are an attractive candidate for power applications because of their high efficiency and benign emissions [1–3]. The thin organic proton exchange membrane in this type of fuel cell works as both an electrolyte and gas separator. Nafion, a perfluorinated polymer, is the most common membrane in PEM fuel cells. Nafion has a polytetrafluoroethylene backbone and perfluorinated side chains with terminating sulfonic acid groups (-$SO_3H$) [1].

The efficiency of polymer electrolyte membranes for fuel cell applications is governed by the proton conductivity, which is determined by the proton mobility and proton concentration in the aqueous phase of the membrane. Excess water produced in PEM fuel cells at the cathode can limit reactant gas transport. Too little water at the anode can cause the membrane to dry out and lose its conductivity. Maintaining an appropriate water balance within the membrane is critical to ensuring optimal operation of the PEM fuel cell [4,5]. To fully understand water management and the conductivity of the fuel cell membrane, one must determine the proton conductivity, water diffusion coefficient, and electro-osmotic drag coefficient—all as functions of water content in the membrane [6].

Numerous phenomenological models of the PEM in fuel cells have been created [7,8]. However, an efficient measurement to directly characterize the spatial distribution of water and water flux across the PEM in an operational PEM fuel cell is still lacking. The Nafion microstructure is known to be anisotropic [9–11], which means that functional studies across the Nafion thin film are essential. Some model functional studies have examined Nafion alteration lengthwise. However these studies ignore the anisotropy and are less directly connected to the membrane function [12].

Two experimental approaches to measuring water distribution across the Nafion membrane in operational fuel cells have been reported in the literature: neutron radiography [13] and traditional $^1$H MRI with frequency encoding [14–16]. Sample alignment difficulties with neutron beam radiography limit the spatial resolution across the Nafion membrane [17]. Difficulty accessing the experimental apparatus also limits the utility of this approach. For traditional $^1$H MRI frequency encoding, conductive materials in the fuel cell will screen the local magnetic field $B_1$, and introduce $B_0$ distortion due to different volumetric magnetic susceptibilities, generating image artifacts [18]. Although some MR techniques can minimize the loss of image quality [19], conventional frequency encoded MR imaging methods are not well suited to high resolution imaging. The spatial resolution provided by conventional

* Corresponding author. Fax: +1 506 453 4581.
*E-mail address:* bjb@unb.ca (B.J. Balcom).
[1] Current address: Department of Systems and Computer Engineering, 1125 Colonel By Drive, Carleton University, Ottawa, Ont., Canada K1S 5B6.

1090-7807/$ - see front matter © 2008 Elsevier Inc. All rights reserved.
doi:10.1016/j.jmr.2008.07.011

MRI and neutron radiography, on the order of tens of μm, is inadequate. Conventional $^1$H MRI frequency encoding has an implicit $T_2$ weighting which makes quantitative water content maps problematic [14–16].

Bulk magnetic resonance measurements have provided valuable insight into the molecular dynamics and transport properties of water in Nafion. MacMillan [20,21] explored the MR relaxation times of water in Nafion as functions of relative humidity (RH) and temperature; Zawodzinski [22] employed pulsed field gradient spin echo experiments to investigate the water diffusivity in Nafion; Codd [23] investigated the heterogeneity of Nafion membranes by studying the variation of $T_2$ and diffusion coefficient when immersed in binary methanol-water solvent mixtures; Baker [12] examined lengthwise changes in Nafion water content in a model electro-active polymer device. The lithium modified Nafion in this case featured long lived $T_2$ lifetimes, an order of magnitude longer than native Nafion. Feindel [18,24] and Minard [19], employed custom built fuel cells to spatially resolve the water content in Nafion membranes in 2D MRI images. Their goals were to explore water flooding effects and the distribution of active areas in an operational fuel cell.

In the current study, the water content is mapped across a Nafion 1110 membrane intended to mimic the wetting and drying boundary conditions of an operational fuel cell. The pure phase encode MRI measurement is a multiple echo centric scan spin echo single point imaging measurement, which is abbreviated by the acronym DHK SE SPI [25]. It has a theoretical resolution, diffusion limited, of 2 μm. In previous work we achieved 4 μm nominal resolution across isolated Nafion 117 membranes with an acquisition time of tens of seconds [25].

In this work, we simplify the water transport problem in a mock fuel cell, removing the complications associated with an operating fuel cell. The membrane boundary conditions are externally controlled in these studies whereas they are internally controlled and less well known in a real fuel cell.

Three different, well-controlled, boundary conditions were established for studying the water gradient across Nafion membrane samples. Spatially and temporally resolved water content and $T_2$ maps reveal surprising trends in Nafion wetting/drying behavior. The resulting profiles and the corresponding $T_2$ values are interpreted based on the physical model presented by Weber and Newman [26,27].

## 2. Theory

### 2.1. Multi-echo centric scan spin echo single point imaging (Multi-echo DHK SE-SPI)

The pulse sequence, Fig. 1, is a relatively new MRI methodology for high resolution imaging of thin film samples, where the MR signal intensity is inherently low [25]. Averaging the cross section of the sample while encoding along the depth direction, referenced to the axis system of Fig. 2, significantly improves the signal to noise ratio (SNR).

This centric scan technique, with an extended recovery time preceding the $k = 0$ RF pulse, is immune to $T_1$-weighting [28–30]. Therefore, the spatially resolved image intensity is simply,

$$S(y) = \rho_0(y) \cdot \exp\left(-\frac{n\mathrm{TE}}{T_2(y)}\right), \quad (1)$$

where $n$ is the echo number, and TE is the echo time. $S(y)$ is the image intensity defined by the product of the spin density, $\rho_0(y)$, and $T_2$ weighting in the exponential term.

Using a surface coil for the MR measurements produces an inherently inhomogeneous $B_1$ field. The consequence is non-ideality in the 90° and 180° RF pulses. In such a circumstance, the measurement may lead to a mixture of magnetization components [31], an accumulation of phase errors, and a loss of signal. In addition to the techniques implemented in Ref. [25], the current work employs composite RF pulses [32–34] for the 180° pulses.

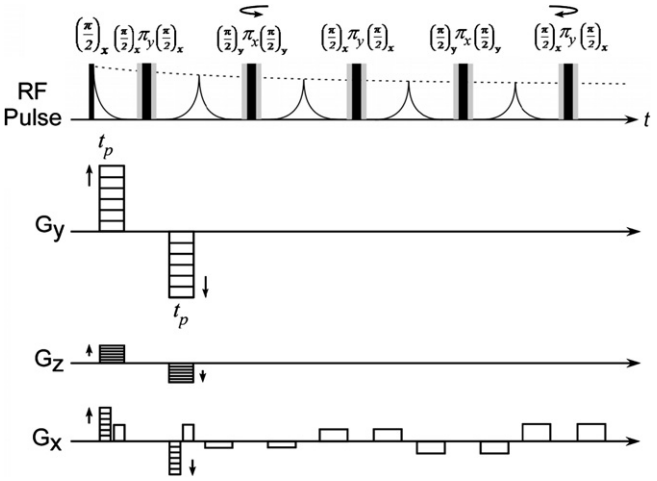


**Fig. 1.** First half of the multi-echo centric scan spin echo single point pulse sequence. The second half acquires the negative k space data points. A time $5T_1$ before acquisition of each half of k space ensures no $T_1$ contrast in the image. Bipolar phase encode and spoiling gradients are employed. The principal spatial encoding gradient is $G_y$. The $G_z$ and $G_x$ gradients are used in linear combination with $G_y$ to ensure the imaging axis is orthogonal to the sample plane. 16 echoes are acquired for $T_2$ mapping.

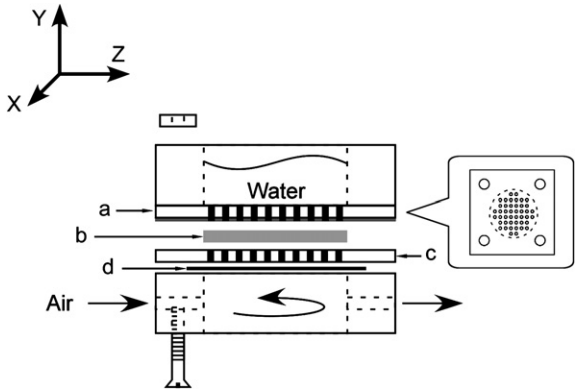


**Fig. 2.** Schematic of the mock fuel cell with wetting/drying boundary conditions. The Nafion layer, b, is held (in the general case) between two perforated plates (a and c), whose structure is illustrated in the inset at right. Plate (a) is fabricated from copper plated PC board. Plate (c) is made of G10 fiberglass. A water reservoir sits on top of plate (a) with a drying chamber underneath plate (c), also made from G10 fiberglass. Beneath plate (c), a 1.8 cm diameter surface coil (d) was installed. The entire apparatus was held together by 4 brass screws with a controlled torque applied.

### 2.2. $T_2$ Measurement

We anticipate from the literature [20,21], and prior experience [25], that the MR relaxation times in Nafion will vary with water content. With a gradient of water content across the membrane, there will also exist a gradient of relaxation times.

To generate quantitative water content maps we must have the ability to rapidly map $T_2$. The multi-echo DHK SE SPI measurement generates a rapid series of $T_2$ weighted profiles according to Eq. (1). By fitting each pixel in the profile series to Eq. (1), it is possible to spatially resolve both $T_2$ and the local proton density, $\rho_0(y)$, corresponding to the water content. It is known that $T_2$ varies in the

range of 6–50 ms, as the Nafion increases in moisture content to saturation [20,21,35,36]. The echo time should be shorter than $T_2$ for high quality measurements. Our minimum echo time, TE = 5.5 ms, was limited by gradient switching times, with the maximum gradient, 50 Gauss/cm.

The conventional view of water in Nafion is that there will exist both bound water and bulk-like water. The large population of bulk-like water exists in discrete clusters associated with acid sites and dominates the global relaxation time behavior [20,21]. Fast magnetization exchange, through water exchange or magnetization cross-relaxation, of the water molecules from multiple sites yields single exponential magnetization decays [20,21]. In this paper, single exponential fitting was implemented to determine $T_2$ and proton density values for all measurements.

### 2.3. Surface coil with RF shielding

As shown in Fig. 2, a water reservoir on top of the Nafion layer saturates the sample, when desired, to ensure a fully wet boundary condition. The excitation profile of the surface coil will extend into the water reservoir, unless screened. Removing the signal from the water reservoir is accomplished by placing a perforated PC board between the reservoir and membrane. The perforations allow the water to flow freely, while the copper effectively shields the reservoir from the RF coil.

The presence of the RF screen will alter the $B_1$ field distribution within the Nafion layer. A numerical simulation was carried out to predict the influence of the perforated conductive layer on the lateral sensitivity and depth sensitivity of the measurement. The geometry and scale of the simulation correspond to that of the real apparatus. Fig. 3(a) shows a plot of the simulated $B_1$ intensity, 1.6 mm above the surface coil and below the RF barrier, in the ZX plane. Only the $B_1$ component orthogonal to $B_0$ is plotted. Attenuation of the $B_1$ field at the centre of the coil is obvious. However, in the peripheral area adjacent to the coil, there still exists a relatively strong $B_1$ field. This field will be oriented perpendicular to both the coil axis and the direction of RF current flow. Consequently, $B_1$ will be parallel or anti-parallel to $B_0$ in the vicinity of the top and bottom of the ring, as indicated by the intensity voids in these regions. Fig. 3(b) shows an experimental 2D lateral image of the Nafion membrane. The signal at the center is heavily attenuated, while that in the periphery is quite strong. As predicted from Fig. 3(a), there is a signal void at top and bottom of the image. Despite the inhomogeneity of the excitation in the plane of the coil, quantitative depth imaging is still possible due to the symmetric lateral averaging of the measurement.

Due to the pure phase encoding MR technique, the resulting images should be free from most image distortions [37,38]. A control experiment was undertaken to explore the influence of the RF screen on the image and any potential artifacts including depth dependent sensitivity. A composite phantom, three layers of saturated Nafion 117, 570 μm in thickness, was imaged with and without the RF screen above the sample. The profiles of this sample, Fig. 3(c), show no obvious geometric differences, with and without the RF screen. The sensitivity is attenuated by the presence of the RF screen. In our mock fuel cell experiments, the signal from the water reservoir will be blocked by the copper screen, without compromising the quantitative nature of the experiment.

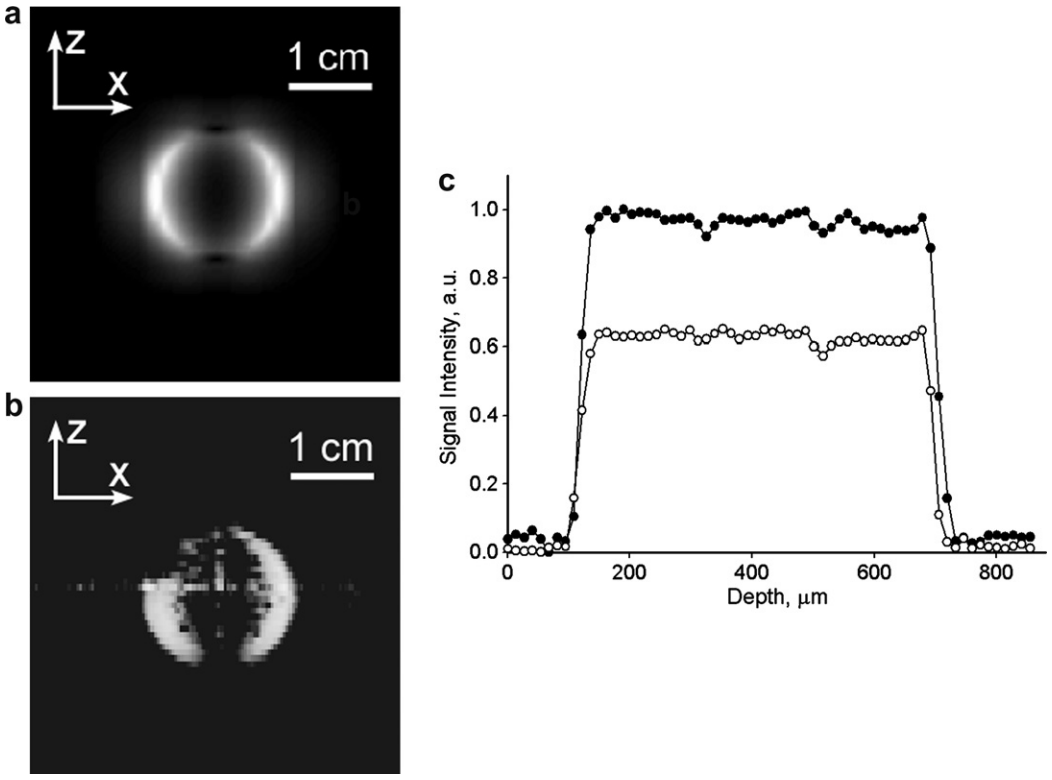


**Fig. 3.** (a) $B_1$ magnetic field simulation of the surface coil RF field. Only the field components in the XY plane are considered. The amplitude distribution of the $B_1$ field, orthogonal to $B_0$, is altered due to the RF screening effect of the copper PC board, 2 mm above the probe. The plot shows the field in the ZX plane, with the PC board, parallel to the coil. Light areas represent higher field intensity. A pronounced lateral inhomogeneity due to the effect of the shield is observed. (b) Experimental 2D lateral image acquired from 2D SE SPI (spatial encoding with $G_x$ and $G_z$). The Nafion image is a circular ring signal void at the top and bottom, as predicted from (a). The symmetric distortion of the RF field, the simulation (a) and experiment (b), yields a largely uniform sensitivity in the $y$ direction through the sample. (c) 1D depth profiles of a composite saturated Nafion 117 sample, with the RF screen present (○) and absent (●). No apparent image distortions are observed. The RF screen decreases the experimental sensitivity as anticipated, but does so uniformly at all depths.

### 2.4. Membrane structure model

The physical model of Weber and Newman [26,27] provides a useful framework to interpret our MRI experiments. The Nafion membrane has a hydrophilic part—the sulfonic acid sites and a hydrophobic part, the polymer matrix, which is essentially Teflon. In addition, the physical connections between adjacent water clusters are assumed to be elastic channels.

The Weber–Newman model is illustrated schematically in Fig. 4. At low water content, water solvates acid groups at small discrete sites. With additional water, Fig. 4b, clusters grow and bulk-like water appears in the clusters. Hydrophobic interconnections exist between clusters. Nafion in equilibrium with saturated water vapor, Fig. 4c, forms a comprehensive cluster-channel network. Nafion in equilibrium with liquid water, Fig. 4d, is assumed to form swollen water filled channels between clusters. The water content of the Nafion is higher when in contact with liquid water as compared to saturated water vapor—a fact known as Schroeder's paradox.

With membranes pretreated by water saturation, the membrane channels are fully expanded. The water clusters, centered around an agglomeration of sulfonic acid sites, are also saturated and the membrane swells. Membrane swelling results from a complex interplay between the affinity of the polymer and ionic sites for water and the resistance of the membrane's structure and crystallinity to volumetric expansion [1]. When the Nafion commences drying, channels collapse, the cluster size and volume will decrease, and the membrane shrinks.

### 2.5. $T_2$ trends based on Weber's structural model

In this study, the Nafion sample is dynamic. Consequently, the spin-spin relaxation time, $T_2$, must be spatially and temporally resolved to determine the local water content. MacMillan et al. [20] have studied the MR relaxation times of static Nafion membranes as a function of water content and determined that the MR relaxation times of Nafion vary with the water content. Beyond water content determination, we seek to rationalize trends in $T_2$ through Weber's model.

Single exponential $T_2$ behavior suggests rapid magnetization exchange between different environments. It is natural to invoke a rapid exchange, weighted average model of $T_2$ behavior including water in the channels and water in the clusters.

$$\frac{1}{T_2} = \sum_i p_i \cdot \frac{1}{T_{2,i}}, \tag{2}$$

where, $i$, represents water environments in exchange, each with an associated $T_2$. These environments must include bound and free water in both cluster and channels, with the probability of each sub-population represented by $p_i$.

The weighted average $T_2$ has short $T_2$ contributions from bound water populations and long $T_2$ contributions from bulk like water. Increasing or decreasing the water content will alter $p_i$ and potentially the associated $T_{2i}$ in Eq. (2).

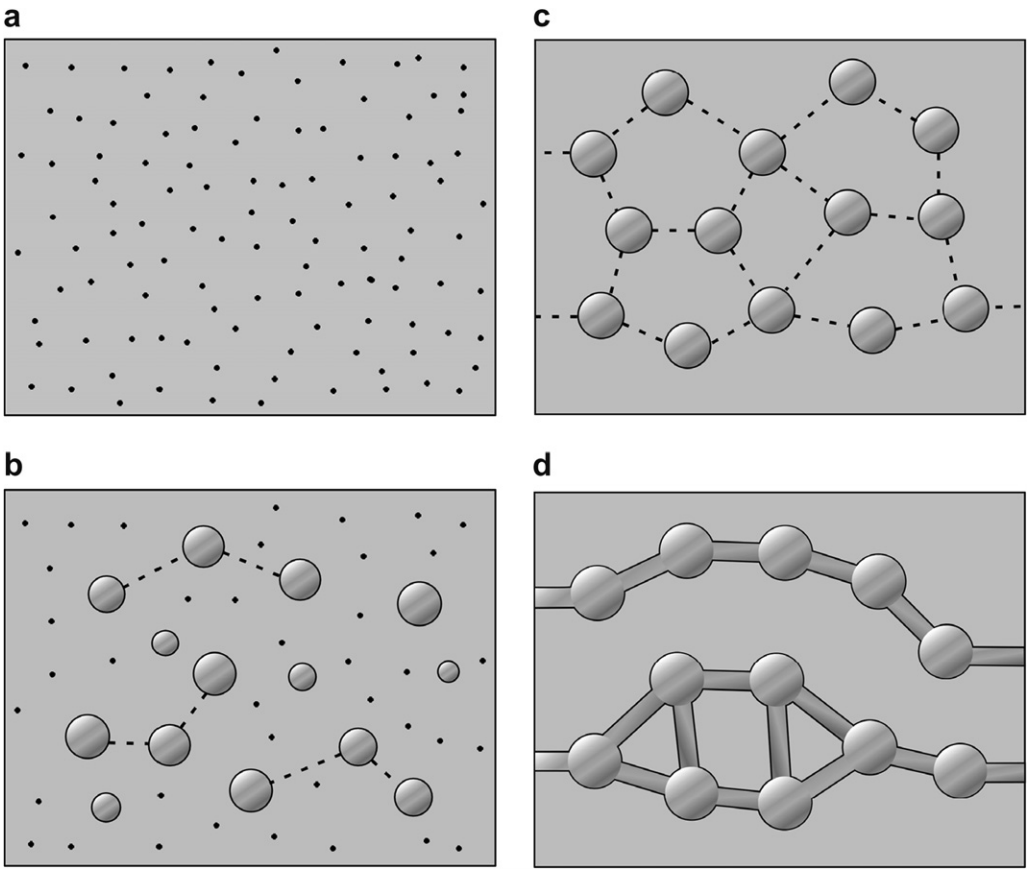


**Fig. 4.** Evolution of the membrane structure as a function of water content, $n$ (moles of water per mole of sulfonic acid sites), in Weber's model, reproduced according to Ref [27]. Four stages, (a), (b), (c) and (d), representing $n = 0$, $n < 2$, $n = 14$, and $n = 22$, are illustrated. In these cross-sectional pictures, the light gray background represents the fluorocarbon matrix, the solid black line represents the polymer side chain, the shining gray represents the liquid water, and the dotted line represents the elastic channels.

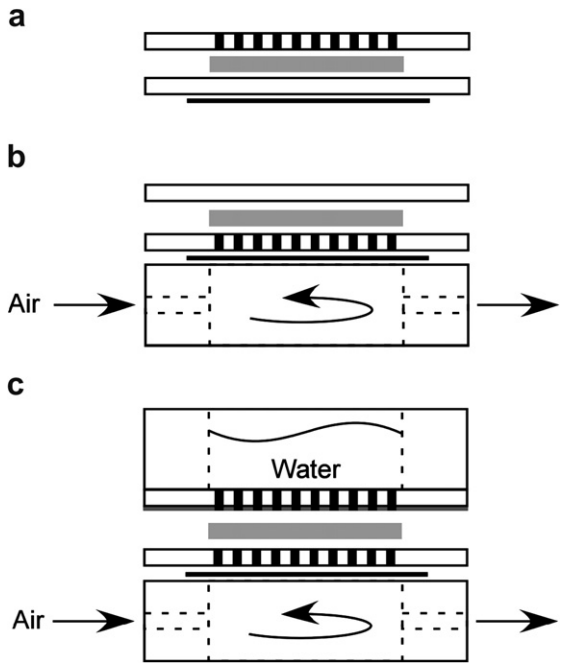


**Fig. 5.** Schematic of the mock fuel cell for three different boundary conditions. (a) Passive drying. The Nafion film is sandwiched between an impermeable plate at the bottom and a perforated plate on the top, T: 15 °C, RH: 20%. (b) Active drying. Similar to (a) but with the perforated plate below the Nafion layer with a dry gas flow through the drying chamber. T: 19 °C, RH: 12%. (c) Wetting and drying boundary conditions. The mock fuel cell mimics the Nafion boundary conditions in an operational PEM fuel cell. The cell was described in Fig. 1. T: 19 °C, RH: 12%.

## 3. Results and discussion

### 3.1. Wetting/drying boundary conditions

Unlike operating fuel cells, the mock fuel cell does not form a complete electrical circuit; it has no catalyst, no gas diffusion layers and no chemical reaction. The mock fuel cell does however provide well-controlled boundary conditions. The evolution of the water content across the Nafion membrane was investigated with different wetting/drying boundary conditions.

(1) Passive drying, Fig. 5(a). The Nafion film is sandwiched by an impermeable plate at the bottom and a perforated plate on the top, which exposes the sample to air. Water will diffuse out of the membrane with slow drying.
(2) Active drying. A dried gas flow was employed to create a more vigorous drying experiment, Fig. 5(b). An impermeable plate seals the sample on the top and a perforated plate connects the sample and a gas chamber underneath. Air flow, with constant RH, through the gas chamber will maintain well mixed, dry, boundary conditions and increase the rate of drying.
(3) Controlled wetting and drying. Fig. 5(c), a water reservoir on the top of the Nafion layer was employed to maintain saturation and a dried gas flow underneath was employed for drying. In this case, we anticipate water flow into the top of the membrane to reach a steady state with drying from below.

Active and passive drying experiments may be considered simple preliminaries for the more complicated, but more realistic, wetting/drying experiment.

### 3.2. Passive and active drying

Since no water reservoir was used in the passive and active drying experiments, the RF shielding of Fig. 2 was omitted.

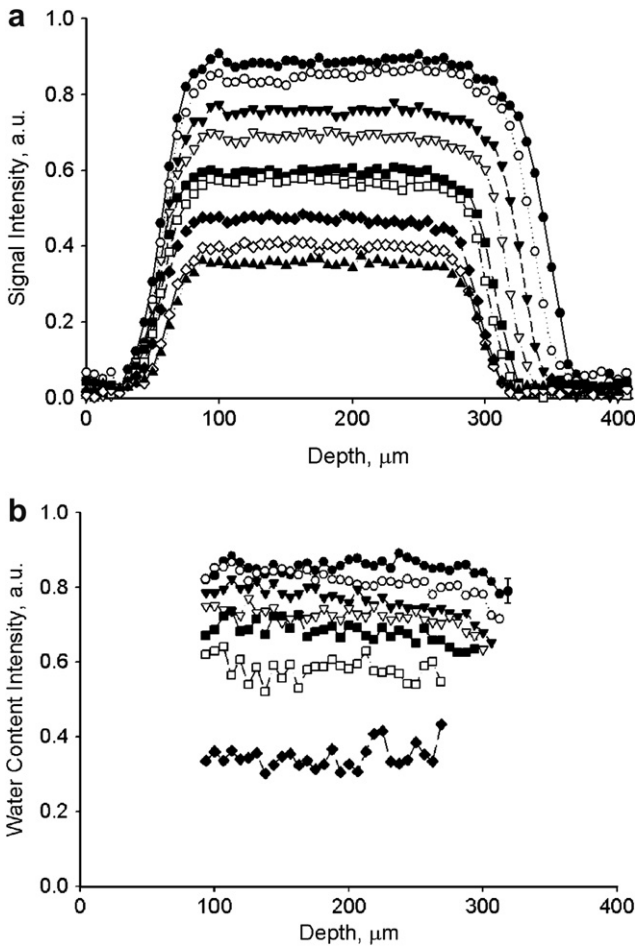


**Fig. 6.** (a) Water content across the Nafion membrane undergoing passive drying, Fig. 5(a). Nine profiles spanning 24 h illustrate the drying process. Profiles correspond to the first echo images. Experiments (•), (○), (▼), (▽), (■), (□), (♦), (◇), (▲) correspond to experimental times of, 0.27, 1.8, 3.4, 4.9, 7.0, 9.1, 11.1, 15.6 and 21.5 h. The left side of the profiles correspond to the sealed side of the sample, and the right side is the drying boundary. The sample shrinks in thickness for the first 15 h. (b) True water content maps of the drying profiles determined by relaxation time mapping. It is not possible to determine $\rho_0(y)$ at the edges of the profiles. Experiments (•), (○), (▼), (▽), (■), (□), (♦) correspond to experimental times of, 0.13, 1.5, 3.3, 4.8, 6.7, 17.8, 23.3 h. The water content is quasi uniform and decreases with time. The typical experimental uncertainty due to $\rho_0$ fitting is illustrated by the representative error bar in the top profile at far right.

Fig. 6 reports the image profiles, (a), and the water content profiles after $T_2$ fitting, (b), of the passive drying experiments. The experiment duration was approximately 24 h with more than 500 sets of multi-echo profiles acquired, at approximately 2.5-min intervals.

In Fig. 6(a), 9 discrete profiles have been chosen to reveal trends in water content across the Nafion. There is a very obvious shrinkage observed as the drying proceeds. In addition, the signal intensity in each profile is uniform, indicating effective redistribution of water inside of the sample with drying. Fig. 6(b) reports water content $\rho_0(y)$. The water content is quasi uniform, but with a discernable decrease toward the drying side, and decreases with time. We are not able to determine $\rho_0(y)$ at the edges of the profile due to difficulty fitting the data.

The active drying experiment, Fig. 7, is similar to that of passive drying, but with a more rapid water loss. Once again the membrane shrinks as it dries, Fig. 7(a). The profile intensity is reasonably uniform at each time point, although the intensity decreases rapidly with time. The true water content $\rho_0(y)$, Fig. 7(b), is quasi uniform, but with a discernable decrease toward the drying side,

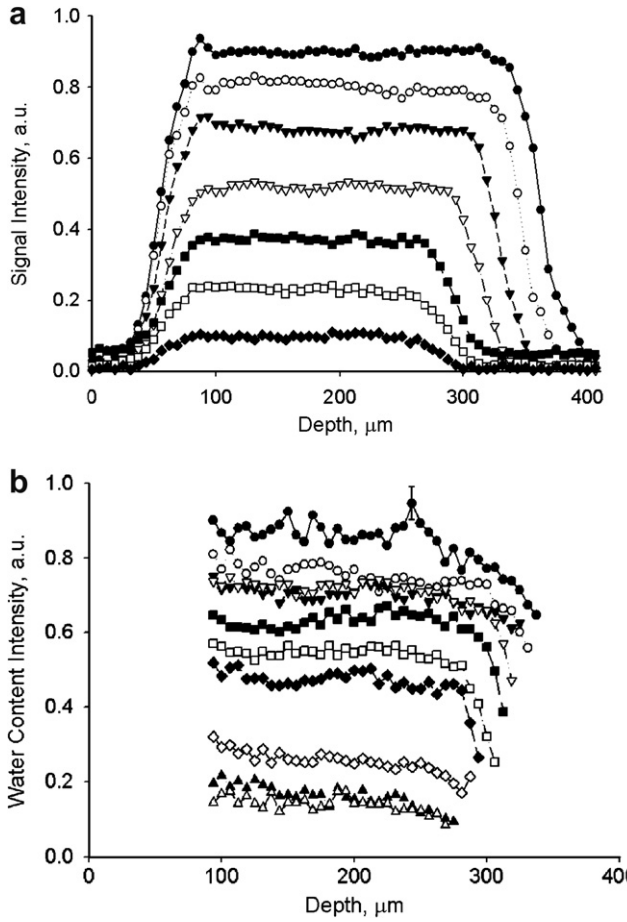


**Fig. 7.** (a) Water content across the Nafion membrane undergoing active drying, Fig. 5(b). Experiments, (●), (○), (▼), (▽), (■), (□), and (♦) correspond to experimental times of, 0.13, 0.5, 1.2, 2.5, 3.0, 4.2, and 5.6 h. The membrane shrinks as it dries, with the profile intensity quite uniform, although the intensity decreases with time. (b) True water content profiles determined by relaxation time mapping. Experiments (●), (○), (▼), (▽), (■), (□), (♦), (◇), (▲), and (△) correspond to experimental times of, 0.1, 0.4, 0.8, 1.2, 1.5, 1.9, 2.4, 2.9, and 3.8 h. The water content is once more essentially uniform across the profile, but decreases with time. At right of the profiles, there may be an indication of the development of a drying front as the membrane shrinks. The typical experimental uncertainty due to fitting is illustrated by the representative error bar in the centre of the top profile.

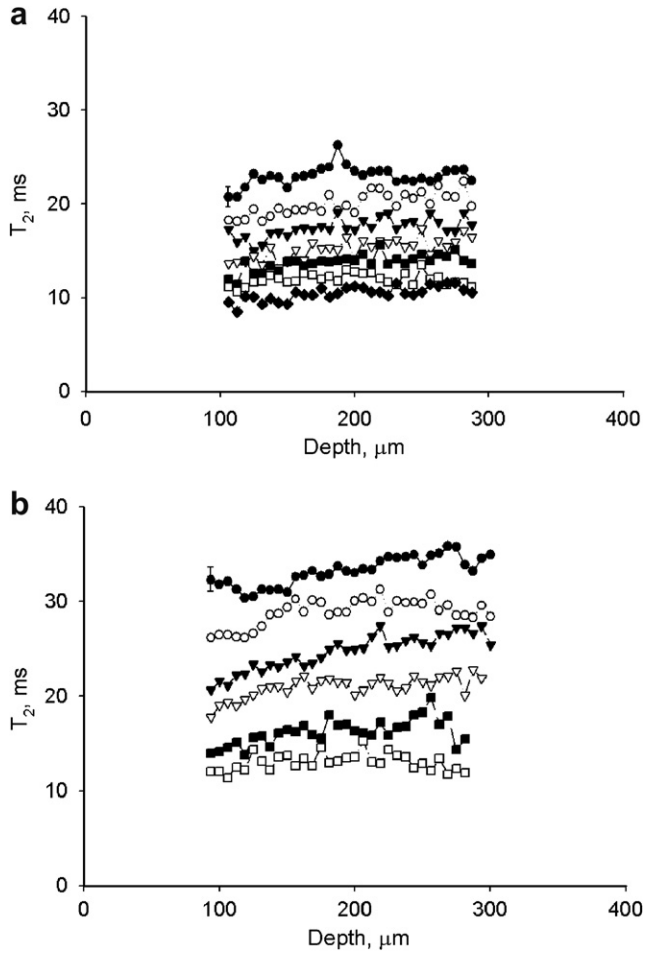


**Fig. 8.** Spatially resolved $T_2$ values for passive and active drying experiments determined from multi-echo imaging experiments. (a) $T_2$ mapping during passive drying. Experiments (●), (○), (▼), (▽), (■), (□), (♦), correspond to experimental times of, 0, 2.2, 4.4, 6.7, 8.9, 11.1, 13.3 h. The $T_2$ values decrease with time, but trend upward close to the drying side at right. (b) $T_2$ mapping during active drying. We display time averaged $T_2$ values in a finite time window, 13.3 min, 5 profiles, for active drying. No such averaging was employed in (A). Experiments (●), (○), (▼), (▽), (■), (□) correspond to time windows of, 0.22–0.44, 1.1–1.5, 1.8–2.0, 2.2–2.4, 3.1–3.3, 4.0–4.2 h. The trend in $T_2$ values is similar to the passive drying case above. Typical uncertainties in the fit $T_2$ are illustrated by the error bar in the top left data point in both (a) and (b).

and decreases with time. There is some indication of the development of a drying front as the membrane shrinks. As mentioned in the theory section, shrinkage of the Nafion sample arises from a decrease in the water cluster size. In the passive/active drying experiments, we observe that the rate of water redistribution is much faster than the rate of systematic water loss.

Fig. 8 presents the measured $T_2$ from passive (A) and active (B) drying experiments. In each profile, Fig. 8(a), $T_2$ was higher on the drying side than that on the sealed side. For the case of active drying, profiles in finite time windows, set to approximately 13 mins, were averaged to increase the SNR, shown in Fig. 8(b). Similar to passive drying, $T_2$ on the drying side was larger than that on the sealed side, with the spatial trend in $T_2$ more pronounced in the active drying case.

In both experiments, as the Nafion membrane was exposed to the air, on the drying side fewer channels with high water content will exist compared to the sealed side of the membrane. The change in probabilities $p_i$ and the time constant $T_{2i}$ in Eq. (2) yields an increase in $T_2$ across the profile from the wet side to dry side. We hypothesize that collapse of the channels linking clusters on the dry side removes short $T_{2i}$ populations from the weighted average $T_2$ yielding a longer $T_2$ value. It is reasonable to assume the $T_2$ of water in the channel environment will be more restricted in motion and therefore of shorter $T_2$.

In addition, for both experiments the $T_2$ decreased with time. Previous work by MacMillan [20,21], suggests decreased water content would result in a decreased average $T_2$. MacMillan's work however relied on Nafion samples at equilibrium unlike the present study which is dynamic. In addition, it is well known that Nafion undergoes a micro-structural rearrangement following perturbation with time constants of hours [39–43]. We believe this ill-defined but very real ageing effect, not accounted for in Weber's model, is connected with the $T_2$ decrease we observe with time. Morphological changes of this type are supported by the necessity to pre-treat Nafion to achieve long $T_2$. Such changes are required to understand the $T_2$ evolution of the wetting/drying experiment of Section 3.3.

The lengthy duration of MRI gradient adjustment, necessary to optimize image resolution [25], on the order of an hour, likely explains the difference in initial $T_2$ of Fig. 8(a) and (b).

For both the passive and active drying experiments, by integrating signal from the central part of each profile and plotting this as a

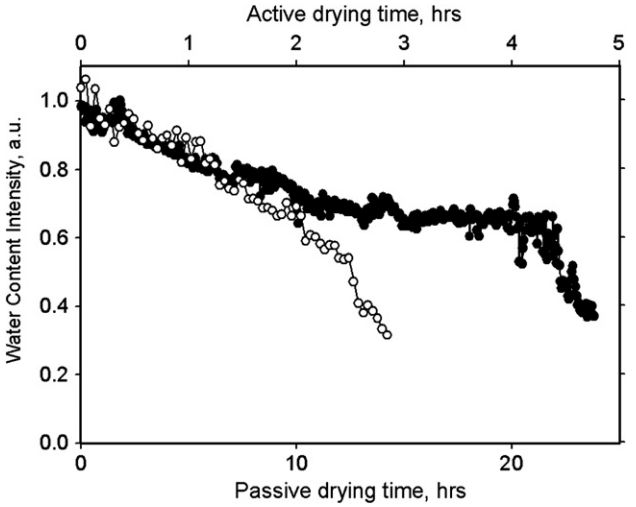


**Fig. 9.** The water content of Nafion in the passive and active drying cases as a function of time. The data is acquired by averaging the image intensity from the central, uniform, part of the water content profiles. (•) and (○), represent passive, and active drying cases, respectively. Although the active drying sample changes must faster, these two traces show a similar discontinuity at approximate 50% relative water content.

function of time, we can investigate the decrease in the signal intensity and the water content with time, as shown in Fig. 9. For the passive drying case, we observe a break point at about 21 h where the nature of the drying changes. The break occurs at 2.5 h for active drying. The break point in each case occurs at approximately 50–60% water content.

Shrinkage of the membrane as it dries is mainly from the loss of the bulk water in the clusters. For a fixed resolution, the signal decrease of each pixel will be attenuated because the film shrinks as it dries increasing the number of water clusters per pixel even as the water content per pixel decreases. The break point indicates the moment when the membrane stops shrinking [20]. Thereafter, the water loss is directly reflected in the profile intensity.

### 3.3. Wetting and drying

The wetting/drying experiment mimics the boundary conditions in an operating fuel cell. One side is fully saturated mimicking the oxidation-reduction reaction boundary condition where water is produced in the fuel cell. The other side is drying mimicking the boundary condition where water is removed through the electro-osmotic drag mechanism.

To the left side of the experimental profiles, in Fig. 10(a), a small signal from the water reservoir is observed, due to incomplete RF screening. On the right there is an obvious 'shoulder' to the profile intensity variation. In the center the profiles are quasi constant in amplitude but decrease with time. Unlike the cases of passive and active drying, no membrane shrinkage occurs until the water reservoir is dry. The decreasing profile intensity, Fig. 10(a), generated from the first echo, as the function of time, suggests a $T_2$ variation with time. Fitting the data to determine $\rho_0(y)$ then averaging data within a time window of 3.4 h, 20 profiles, Fig. 10(b) clearly shows a systematic variation in water content across the membrane with a minor overall decrease in water content. Clearly the decrease is due to $T_2$ changes and an aging effect.

Fig. 11 illustrates 5 $T_2$ profiles, as a function of depth, averaged within a time window of 50 mins. The significantly different boundary conditions in the wetting/drying case yielded more collapsed channels on the drying side than on the wetting side, which yields a longer local $T_2$, as expected, Fig. 10. No membrane shrinking was observed until the water in the reservoir was empty indicating the volume of the clusters was essentially constant in time.

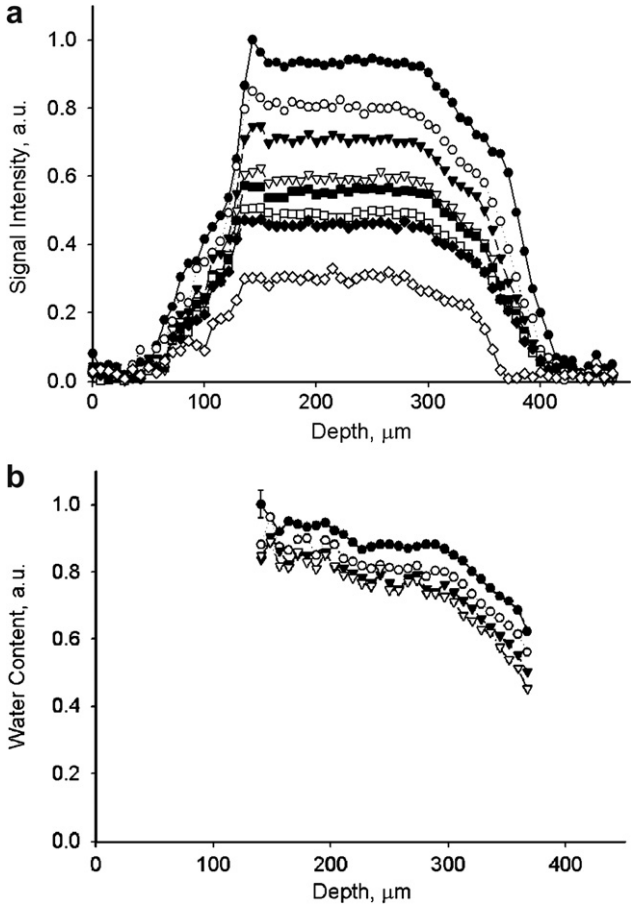


**Fig. 10.** (a) Water content across the Nafion membrane undergoing wetting/drying, Fig. 5(c). Experiments (•), (○), (▼), (▽), (■), (□), (♦), (◇) correspond to experimental times of 0.17, 1.9, 4.6, 8.1, 11.0, 14.0, 16.3, 18.5 h. The water reservoir is at the left in the profiles with the drying chamber at the right. At the bottom left of the profiles, there exists some residual signal from the water in the perforations of the PC board shield. At the right top corner, the 'shoulder' is pronounced. The water reservoir emptied after 18.5 h with an obvious drop in signal intensity at that point. (b) 4 averaged water content profiles from 20 profiles, 3.4 h. Experiments (•), (○), (▼), (▽) correspond to the average from the experimental time range of 0–3.4, 3.4–6.8, 6.8–10.2, 10.2–13.6 h. The non-uniform profiles present two different regimes of water content. Water content decreased over 20 h, due to an aging effect of the membrane. A clear drying front is observed at the drying side. The typical experimental uncertainty due to fitting is illustrated by the representative error bar in the top profile at the far left.

We also observe a distinct trend of overall $T_2$ decrease in the profiles with time. As in the passive and active drying experiments, we believe the overall $T_2$ decrease is due to a micro-structural rearrangement of the Nafion which is well known from a variety of other non-NMR studies [39–43].

To the best of our knowledge this is the first spatially and temporally resolved NMR observation of this phenomenon. Future MRI studies of fuel cell operation may be able to correlate electrochemical performance with water content and $T_2$ variation in the Nafion membrane.

## 4. Conclusion and future work

This paper describes measurements of the water content variation across a Nafion membrane inside a mock fuel cell, under different boundary conditions. Three cases, passive drying, active drying and wetting/drying, were investigated.

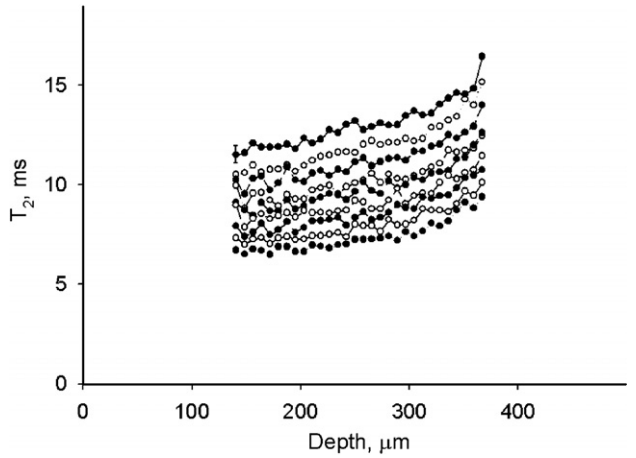


**Fig. 11.** Spatially resolved $T_2$ values for wetting/drying experiments determined from multi-echo imaging experiments. Nine averaged $T_2$ profiles, (5 image acquisitions, 50 min) span the full duration of the experiment, 18 h. Symbols (•) and (○) correspond to alternate experiments. $T_2$ decreases with time, but increases from the wet side to the dry side of the membrane. The typical fitting uncertainty is illustrated by the representative error bar in the top profile at the far left.

Water content maps, at high resolution, were attained with $T_2$ mapping. Spatial and temporal variation of the Nafion $T_2$ proves that $T_2$ mapping is critical to generating quantitative water content maps in these systems.

Water inside the Nafion membrane is highly mobile allowing for fast redistribution. Lacking a water supply, the membrane will shrink as it dries. $T_2$ values increase in all cases from the wet to dry side of the membrane. $T_2$ values in all cases decrease as a function of time, reflecting an aging phenomenon.

Measurements of this type will be used to validate existing numerical models of water transport in Nafion and similar membranes. The experimental techniques employed in this study can be implemented to investigate operational PEM fuel cells.

## 5. Experimental

### 5.1. Chamber design

The mock fuel cell chamber, 3 cm × 3 cm, was shaped from G10 fiberglass (McMaster-Carr, Cleveland, OH). The RF shield plate was cut from fiberglass based PC board, with 50-micron-thick copper cladding. All perforated plates were 1/16″ in thickness. The water reservoir and gas chamber frame was 1/4″ thick. The assembly was embedded in a 1 cm thick Teflon sheet and placed in a copper covered Plexiglas tube.

### 5.2. Sample preparation

The sample film, Nafion 1110, 250 μm thick, was purchased from Ion Power (New Castle, DE). The Nafion 1110 was cut to a 2 cm diameter circle, pretreated by heating in 3–5 wt.% $H_2O_2$ solution at 80 °C for 1 h. The sample was then rinsed in deionized water at 80 °C for 1 h, then, heated in 0.5 M $H_2SO_4$ at 80 °C for 1 h. The sample has finally cleaned by prolonged heating in deionized water at 80 °C for 1 h, to remove any possible chemical residues. The basic procedure was based on the work of Jalani [44] and Moore [45].

### 5.3. MRI details

The Multi-echo DHK SE SPI experiment was implemented on a Nalorac (Martinex, CA) 2.4 T 32 cm i.d. horizontal bore superconducting magnet. A water cooled 7.5 cm i.d. gradient set driven by Techron (Elkhart, IN) 8710 amplifiers, which provided 50 Gauss/cm maximum gradients, was employed for all experiments. Gradient $G_y$ was chosen to be the principal phase encoding gradient. Gradients $G_z$ and $G_x$ were used as secondary phase encode gradients. Gradient $G_x$ also functioned as a spoiling gradient [25]. The imaging console was a Tecmag (Houston, TX) Apollo for all experiments.

The RF probe, driven by a 2 kW AMT (Brea, CA) 3445 RF amplifier, was a custom built single channel surface coil. The RF resonator was formed from copper tape, cut into a circular shape, 2 cm in diameter, affixed to the surface of the gas chamber, shown in Fig. 2. The RF resonator was tuned to 100 MHz with two capacitors in a standard series-parallel tank circuit.

Due to the finite echo time required to achieve the desired resolution, 8 echoes were acquired from successive experiments of different TE, 5.5 and 8.5 ms, respectively, yielding 16 echo profiles for $T_2$ mapping. The nominal 90° pulse width for passive and active drying experiments was 15 μs. Conductive materials (RF shield) alter the Q, and therefore affect the strength of $B_1$ and RF pulse lengths for 90° and 180° pulses. The nominal 90° pulse length was 24 μs for wetting/drying experiments. In all experiments, $180°_y$ pulses were executed as $90°_x 180°_y 90°_x$ composite pulses. The repetition time (TR) was maintained at 500 ms, which is $>5T_1$ for all echo trains for all k-space points, in all experiments.

The nominal resolution for the passive and active drying measurements was 6.5, and 7.4 μm for wetting/drying experiments, with FOVs of 430 and 490 μm, respectively. The encoding time, $t_p$, was 2.2 ms for passive and active drying cases and 1.8 ms for the case of wetting/drying. Dwell times were set to 200 μs to narrow the filter width in all measurements.

In high resolution depth imaging measurements, the Nafion film can not be exactly positioned at the origin of the gradient $G_y$. Experimental profiles therefore wrap around the field of view (FOV) and are translated to the center of the FOV for display and subsequent data processing.

64 k-space points were collected for 1D depth images and 64 by 64 matrix points for 2D lateral images. In the passive and active drying cases, 2 signal averages were accumulated for each profile, with an acquisition time of 160 s. In the wetting/drying measurement, the acquisition time was 610 s with 8 signal averages. 2D SE SPI was employed to acquire the lateral 2D image, with a 25 min acquisition time and no signal averaging. In the 2D imaging experiment, $G_z$ and $G_x$ were spatial encoding gradients [25].

### 5.4. Numerical simulation of $B_1$ field with RF shield

Simulation of the RF shield effect was undertaken with the CST Microwave Studio (CST, Darmstadt, Germany) finite integral simulation program. The simulation represented the RF coil with a thin circular loop, 20 mm in diameter. The perforated shield in the simulation was geometrically the same as the experimental PC board shield and modeled as perfectly conducting. The RF frequency for simulation was 100 MHz.

## Acknowledgments

B.J.B. thanks NSERC of Canada for operating and equipment grants. B.J.B also thanks the Canada Chairs program for a Research Chair in MRI of Materials (2002–2009). The MRI Centre is supported through an NSERC Major Facilities Access award. We thank R.P. MacGregor for his assistance with the experiments and M. Olive and B. Titus for fabricating the sample holder and RF probe.

## References

[1] W. Wielstich, H.A. Gasteiger, A. Lamm, Handbook of Fuel Cell—Fundamentals, Technology and Applications, John Wiley & Sons, 2003.

[2] R.A. Lemons, Fuel cells for transportation, J. Power Sources 29 (1990) 251–264.
[3] G. Hoogers, Fuel Cell Technology Handbook, CRC Press, New York, 2000.
[4] T.E. Springer, T.A. Zawodzinski, S. Gottesfeld, Polymer electrolyte fuel cell model, J. Electrochem. Soc. 138 (1991) 2334–2342.
[5] T.A. Zawodzinski, C. Derouin, S. Radzinski, R.J. Sherman, V.T. Smith, T.E. Springer, Water uptake by and transport through Nafion® 117 membranes, J. Electrochem. Soc. 140 (1993) 1041–1047.
[6] M. Dresselhaus, G. Crabtree, M. Buchanan, Basic Research Needs for the Hydrogen Economy: Report on the Basic Energy Sciences Workshop on Hydrogen Production, Storage, and Use, Department of Energy, 2003.
[7] M. Eikerling, A.A. Kornyshev, Y. Kharkats, Y. Volfkovich, Phenomenological theory of electro-osmotic effect and water management in polymer electrolyte proton-conducting membranes, J. Electrochem. Soc. 145 (1998) 2684–2699.
[8] G.J. Janssen, A phenomenological model of water transport in a proton exchange membrane fuel cell, J. Electrochem. Soc. 148 (2001) 1313–1323.
[9] K.A. Mauritz, R.B. Moore, State of understanding of Nafion, Chem. Rev. 104 (2004) 4535–4585.
[10] M. Rankothge, Haryadi, G. Moran, J. Hook, L. Van Gorkom, Orientation effects in the deuterium NMR spectroscopy of perfluorinated ionomer membranes, Solid State Ionics 67 (1994) 241–248.
[11] H. Chen, G.R. Palmese, Y.A. Elabd, Membranes with oriented polyelectrolyte nanodomains, Chem. Mater. 18 (2006) 4875–4881.
[12] R.T. Baker, L. Naji, K. Lochhead, J.A. Chudek, *In situ* magnetic resonance imaging of electrically-induced water diffusion in a Nafion ionic polymer film, Chem. Commun. (2003) 962–963.
[13] R.J. Bellows, M.Y. Lin, M. Arif, A.K. Thompson, D. Jacobson, Neutron imaging technique for in situ measurement of water transport gradients within Nafion in polymer electrolyte fuel cells, J. Electrochem. Soc. 146 (1999) 1099–1103.
[14] K. Teranishi, S. Tsushima, S. Hirai, Measurement of water distribution in polymer electrolyte fuel cell membrane by MRI, Therm. Sci. Eng. 10 (2002) 59–60.
[15] K. Teranishi, S. Tsushima, S. Hirai, Membrane thickness effect on PEFC's performance by measurement of water distribution, Therm. Sci. Eng. 11 (2003) 35–36.
[16] S. Tsushima, K. Teranishi, S. Hirai, Magnetic resonance imaging of the water distribution within a polymer electrolyte membrane in fuel cells 7 (9) (2004) A269–A272.
[17] R. Satjia, D.L. Jacobson, M. Arif, S.A. Werner, In situ neutron imaging technique for evaluation of water management systems in operation PEM fuel cells, J. Power Sources 129 (2004) 238–245.
[18] K.W. Feindel, L.P. LaRocque, D. Starke, S.H. Bergens, R.E. Wasylishen, In situ observations of water production and distribution in an operating $H_2/O_2$ PEM fuel cell assembly using $^1$H NMR microscopy, J. Am. Chem. Soc. 126 (2004) 11436–11437.
[19] K.R. Minard, V.V. Viswanathan, P.D. Majors, L.Q. Wang, P.C. Rieke, Magnetic resonance imaging (MRI) of PEM dehydration and gas manifold flooding during continuous fuel cell operation, J. Power Sources 161 (2006) 856–863.
[20] B. MacMillan, A.R. Sharp, R.L. Armstrong, NMR relaxation in Nafion—the low temperature regime, Polymer 40 (1999) 2481–2484.
[21] B. MacMillan, A.R. Sharp, R.L. Armstrong, An NMR investigation of the dynamical characteristics of water absorbed in Nafion, Polymer 40 (1999) 2471–2480.
[22] T.A. Zawodzinski, M. Neeman, L.O. Sillerud, S. Gottesfeld, Determination of water diffusion coefficients in perfluorosulfonate ionomeric membranes, J. Phys. Chem. 95 (1991) 6040–6044.
[23] S.L. Codd, D.T. Howe, J.D. Seymour, E.H. Werre, S.C. Busse, E.S. Peterson, Magnetic resonance microscopy of heterogeneity in polymer electrolyte membranes, Appl. Magn. Reson. 32 (2007) 13–24.
[24] K.W. Feindel, S.H. Bergens, R.E. Wasylishen, The use of $^1$H NMR microscopy to study proton-exchange membrane fuel cells, Chem. Phys. Chem. 7 (2006) 67–75.
[25] A.V. Ouriadov, R.P. MacGregor, B.J. Balcom, Thin film MRI—high resolution depth imaging with a local surface coil and spin echo SPI, J. Magn. Reson. 169 (2004) 174–186.
[26] A. Weber, J. Newman, Transport in Polymer-Electrolyte Membranes I. Physical Models, J. Electrochem. Soc. 150 (7) (2003) A1008–A1015.
[27] A. Weber, J. Newman, Transport in Polymer-Electrolyte Membranes II. Mathematical Models, J. Electrochem. Soc. 151 (2) (2004) A316–A339.
[28] I.V. Mastikhin, B.J. Balcom, P.J. Prado, C.B. Kennedy, SPRITE MRI with prepared magnetization and centric k-space sampling, J. Magn. Reson. 136 (1999) 159–168.
[29] M. Halse, J. Rioux, S. Romanzetti, J. Kaffanke, B. MacMillan, I. Mastikhin, N.J. Shah, E. Aubanel, B.J. Balcom, Centric scan SPRITE magnetic resonance imaging: optimization of SNR, resolution, and relaxation time mapping, J. Magn. Reson. 169 (2004) 102–117.
[30] Z. Zhang, A.V. Ouriadov, C. Willson, B.J. Balcom, Membrane gas diffusion measurements with MRI, J. Magn. Reson. 176 (2005) 215–222.
[31] A.A. Maudsley, Modified Carr–Purcell–Meiboom–Gill sequence for NMR Fourier imaging applications, J. Magn. Reson. 69 (1986) 488–491.
[32] M. Levitt, R. Freeman, NMR population inversion using a composite pulse, J. Magn. Reson. 33 (1979) 473–476.
[33] M. Levitt, Symmetrical composite pulse sequences for NMR population inversion. i. compensation of radiofrequency field inhomogeneity, J. Magn. Reson. 48 (1982) 234–264.
[34] M. Levitt, Symmetrical composite pulse sequences for NMR population inversion. ii. compensation of resonance offset, J. Magn. Reson. 50 (1982) 95–110.
[35] R.C.T. Slade, A. Hardwick, P.G. Dickens, Investigation of $H^+$ motion in Nafion film by pulsed $^1$H NMR and A.C. conductivity measurement, Solid State Ionics 9&10 (1983) 1093–1098.
[36] N. Sivashinsky, G.B. Tanny, The state of water in swollen ionomers containing sulfonic acid salts, J. Appl. Polym. Sci. 26 (1981) 2625–2637.
[37] B.J. Balcom, R.P. MacGregor, S.D. Beyea, D.P. Green, R.L. Armstrong, T.W. Bremner, Single-point ramped imaging with $T_1$ enhancement (SPRITE), J. Magn. Reson. 123 (1996) 131–134.
[38] S. Gravina, D.G. Cory, Sensitivity and resolution of constant-time imaging, J. Magn. Reson. B 104 (1994) 53–61.
[39] G. Gebel, Structural evolution of water swollen perfluorosulfonated ionomers from dry membrane to solution, Polymer 41 (2000) 5829–5838.
[40] V. Barbi, S.S. Funari, R. Gehrke, N. Scharnagl, N. Stribeck, Nanostructure of Nafion membrane materials as a function of mechanical load studied by SAXS, Polymer 44 (2003) 4853–4861.
[41] W. Essafi, G. Gebel, R. Mercier, Sulfonated polyimide ionomers: a structural study, Macromolecules 37 (2004) 1431–1440.
[42] M.-H. Kim, C.J. Glinka, S.A. Grot, W.G. Grot, SANS study of the effects of water vapor sorption on the nanoscale structure of perfluorinated sulfonic acid (Nafion) membranes, Macromolecules 39 (2006) 4775–4787.
[43] L. Rubatat, O. Diat, Stretching effect on Nafion fibrillar nanostructure, Macromolecules 40 (2007) 9455–9462.
[44] N.H. Jalani, P. Choi, R. Datta, TEOM: A novel technique for investigating sorption in proton-exchange membranes, J. Mem. Sci. 254 (2005) 31–38.
[45] R.B. Moore III, C.R. Martin, Chemical and morphological properties of solution-cast perfluorosulfonate ionomers, Macromolecules 21 (1988) 1334–1339.